Telecom-Band Quantum Interference of Frequency-Converted Photons from Remote Detuned NV Centers

A.J. Stolk,[1,2,†] K.L. van der Enden,[1,2,†] M.-C. Roehsner,[1,2] A. Teepe,[1,2] S.O.F. Faes,[1,2] C.E. Bradley,[1,2] S. Cadot,[1] J. van Rantwijk,[1] I. te Raa,[1] R.A.J. Hagen,[1,3] A.L. Verlaan,[1,3] J.J.B. Biemond,[1,3] A. Khorev,[1,3] R. Vollmer,[1,3] M. Markham,[4] A.M. Edmonds,[4] J.P.J. Morits,[1,3] T.H.T. Taminiau,[1,2] E.J. van Zwet,[1,3] and R. Hanson[1,2,*]

[1] *QuTech, Delft University of Technology, Delft 2628 CJ, Netherlands*

[2] *Kavli Institute of Nanoscience, Delft University of Technology, Delft 2628 CJ, Netherlands*

[3] *Netherlands Organisation for Applied Scientific Research (TNO), P.O. Box 155, Delft 2600 AD, Netherlands*

[4] *Element Six Innovation, Fermi Avenue, Harwell Oxford, Didcot, Oxfordshire OX11 0QR, United Kingdom*

(Received 4 February 2022; accepted 13 April 2022; published 21 June 2022)

Entanglement distribution over quantum networks has the promise of realizing fundamentally new technologies. Entanglement between separated quantum processing nodes has been achieved on several experimental platforms in the past decade. To move toward metropolitan-scale quantum network test beds, the creation and transmission of indistinguishable single photons over existing telecom infrastructure is key. Here, we report the interference of photons emitted by remote spectrally detuned NV-center-based network nodes, using quantum frequency conversion to the telecom *L* band. We find a visibility of 0.79 ± 0.03 and an indistinguishability between converted NV photons around 0.9 over the full range of the emission duration, confirming the removal of the spectral information present. Our approach implements fully separated and independent control over the nodes, time multiplexing of control and quantum signals, and active feedback to stabilize the output frequency. Our results demonstrate a working principle that can be readily employed on other platforms and shows a clear path toward generating metropolitan-scale solid-state entanglement over deployed telecom fibers.

DOI: 10.1103/PRXQuantum.3.020359

I. INTRODUCTION

A future quantum Internet [1,2], built using quantum processor nodes connected via optical channels, promises applications such as secure communication, distributed quantum computation, and enhanced sensing [3–5]. In recent years, the generation of entanglement between remote processor nodes has been realized with ions and atoms [6–9], nitrogen-vacancy (NV) centers in diamond [10,11], and quantum dots [12,13]. Moreover, other platforms such as rare-earth-doped crystals [14–16], atom-cloud-based memories [17,18], and mechanical resonators [19] have been used to explore distributed entangled states.

Central to commonly used remote-entanglement generation protocols [6,8–13] is the propagation and interference of single photons that are entangled with stationary qubits in the nodes. Scaling these schemes to many nodes and to long distances poses two main challenges. First, any source of distinguishability between the emitted photons needs to be removed to generate high-fidelity entangled states. Especially for solid-state emitters, this requirement is difficult to meet for a large number of nodes due to variations in the local environment of the emitters. Second, for long-distance connections, photon loss in fibers is a dominant factor determining the rate at which the entanglement generation succeeds. Leading platforms for realizing processor nodes [9,20–24] in a future quantum network have natural emission frequencies in the visible spectrum; fiber losses at these frequencies hinder scaling beyond a few kilometers.

In this work, we show that both challenges can be addressed simultaneously by converting the coherent single-photon emission from NV centers (637 nm) to a single target wavelength in the telecom *L* band (1565–1625 nm) [Fig. 1(a)]. Using the pump lasers to compensate for local detuning and using active stabilization of the frequency of the converted field, we are able to decouple the natural emission wavelength of the emitters from the wavelength used for propagation and

*R.Hanson@tudelft.nl

†These authors contributed equally to this work.

interference and build fully independent modular quantum nodes. We demonstrate that this method enables the removal of spectral offsets over a broad frequency range (> 3 GHz). Moreover, the chosen interference wavelength has low propagation losses over commercially available optical fibers, making it suitable for long-range single-photon transmission.

We validate our approach by measuring quantum interference [26] between telecom photons that are frequency converted from the emission of two remote NV centers that are detuned by more than 100 linewidths. By comparing the data to a detailed model, we extract both the major noise sources and the underlying indistinguishability of the converted NV photons.

II. INDEPENDENT QUANTUM NETWORK NODES

We employ two independently operated quantum network nodes separated by a few meters on different optical tables. The nodes are connected to a midpoint located in two separate 19-in. racks. The relevant elements are depicted in Fig. 1(c). Each node operates a single diamond NV center as stationary qubit, hosted in a closed-cycle cryostat at $T \approx 4\,\mathrm{K}$. The relevant energy levels and optical transitions of the NV qubit are depicted in Fig. 1(b). The spin-reset transition is used for spin initialization into $m_s = 0$ (fidelity > 0.99). We use the transition to the $E_{x/y}$ excited state to generate single photons: a coherent optical π pulse (approximately 2 ns) brings the NV center to the excited state, followed by spontaneous emission (lifetime approximately 12 ns [27,28]). Both setups employ their own lasers and optical components that deliver and collect light to the NV center.

The nodes are equipped with a (nominally identical) quantum-frequency-conversion (QFC) module. Here, the light at 637 nm is converted to 1588 nm via a single-step difference-frequency-generation (DFG) process. This process has previously been shown to preserve entanglement between the photon and an NV-center qubit [29]. The QFC modules are based on waveguides in a periodically poled lithium niobate (ppLN) crystal, where the large nonlinear coefficient facilitates conversion of single photons using a strong 1064-nm pump field. Various remotely controllable components allow for the remote and automated optimization of the QFC modules. While this single-step conversion has the upside of using a prevalent commercially available pump laser, it has the challenge of introducing spontaneous parametric down-conversion noise at the target wavelength by the pump laser due to imperfections in the crystal domains [30].

After free-space filtering to remove the bright pump light, the frequency-converted light is guided to a central midpoint. At the midpoint, a series of filters separate photons at the target wavelength from stabilization light and filter out noise photons. To achieve a high suppression of any broadband background light, we use a two-step filtering process. First, we use a reflection off a narrow band-stop filter of 0.35 nm, followed by transmission through an ultranarrow [a full width at half maximum (FWHM) of approximately 50 MHz] fiber Bragg grating (abbreviated using UNF). The filters are connected via circulators and an in-fiber polarizer is used to ensure optimal performance of the UNF [Fig. 1(b)]. After filtering, we interfere the two paths using a 50:50 beam splitter and detect the photons using single-photon superconducting nanowire detectors (SNSPDs).

III. REALIZING SPECTRAL STABILITY VIA FEEDBACK

For solid-state emitters, the local environment can influence the emission properties directly via electric, magnetic, or strain fields. For instance, for NV centers in nominally low-strain samples, the local strain environment can shift the emission frequency by more than 1000 times the linewidth [31]. While direct tuning of emission wavelength is in principle possible on several platforms, e.g., by strain [32], via static electric fields [10,13], or by using Raman-tuned emission for emitters embedded in a cavity [33,34], the range of tunability is generally limited. Also, direct tuning brings additional complexities in the device fabrication and can add significant experimental overhead.

We show that we can use the QFC process to remove the spectral offset between the NV emission without the need for direct tuning of the optical transition. An analogous scheme has recently been used on spectrally distinct quantum dots [35,36]; a key difference is that the NV-center host diamond also contains a long-lived matter qubit[37] and can function as a processing node in a quantum network [23]. Using resonant-excitation spectroscopy, we find the optical transition frequency used for single-photon generation at each node [Fig. 2(a)]. We observe that these transition frequencies are separated by approximately 3 GHz (about 100 natural linewidths), as shown in Fig. 2(b).

To bring the NV photons to the same target frequency, we realize a scheme that locks the pump laser at each node to the frequency difference between the excitation laser at that node (and hence the NV emission frequency) and a joint telecom reference laser at the midpoint. To achieve this lock, we use a split-off of the excitation laser, offset in frequency by a fixed 400 MHz, as stabilization light [see Fig. 2(d)]. We propagate this stabilization light through the same frequency-conversion path as the NV photons. Due to the frequency offset, the stabilization light is reflected at the UNF, traveling backward toward the first circulator, where it exits [see Fig. 1(c)]. Light from the joint reference laser is inserted at the second circulator, from where it propagates in the opposite direction through the transmission flank of the UNF, also exiting on the first circulator. Here, the interference with the stabilization light

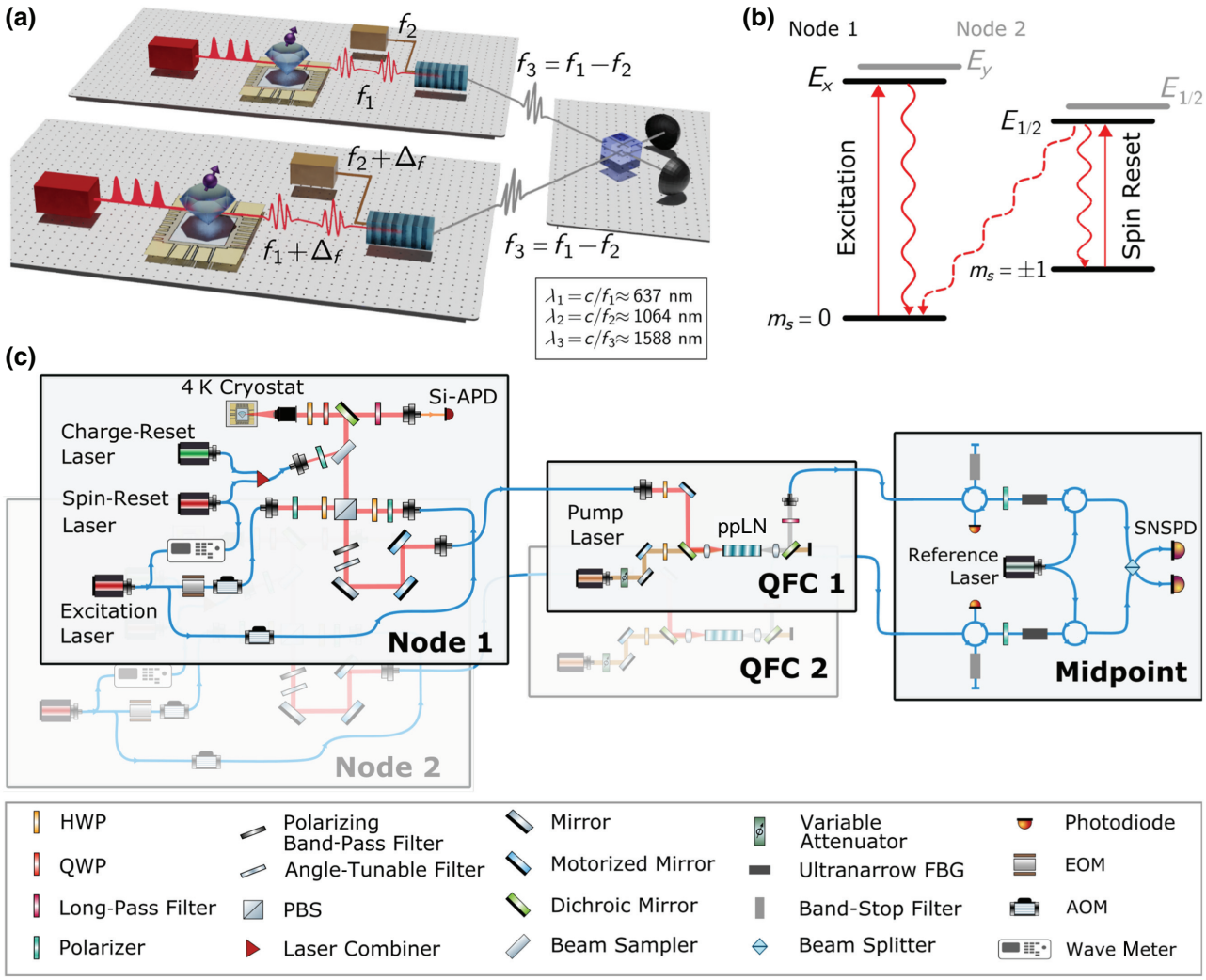

FIG. 1. The layout of the two independent network nodes and the midpoint. (a) A schematic of the main components of the setup. Pulses excite the NV center, which emits single photons through spontaneous decay. The photons are converted to telecom wavelength and guided toward a midpoint placed in the neighboring laboratory, where they interfere on a beam splitter (for more details on optics, see the Supplemental Material [25]). (b) The NV-center level structure, showing the spin levels in the ground state and the relevant optical transitions. The optical transitions of the two nodes have different energies due to local variations in strain (see text). (c) A detailed schematic showing the optics used for full operation of the system. The nodes are identical and no hardware is shared between the systems. Each node has a set of charge reset, spin reset, and excitation lasers, which are modulated, combined, and focused via a high-NA objective onto the NV center. The phonon-side-band (PSB) [zero-phonon-line (ZPL)] emission from the NV center is filtered using frequency (polarization) filtering and coupled into a multi- (single-) mode fiber. The PSB emission is measured locally on an Avalanche Photodiode, while the ZPL emission is sent to the quantum-frequency-conversion (QFC) module. Stabilization light is split off from the excitation path and brought into the single-photon path via a polarizing beam splitter. The QFC module contains remotely controllable optics to align the input, pump, and converted fields to the waveguide on the periodically poled lithium niobate (ppLN) crystal that converts both the single photons and stabilization light. Polarization-maintaining (PM) fibers transport the photons to a midpoint where the single photons are filtered and separated from the stabilization light using a combination of in-fiber filters. The single photons interfere on a beam splitter and are measured by single-photon superconducting nanowire detectors (SNSPDs), while the stabilization light interferes with the reference laser and is measured on a photodiode.

is measured on a photodiode, yielding the error signal for the lock (see the Supplemental Material [25]). We close the loop by applying feedback to the pump laser, imprinting the same frequency shift on both the single photons and stabilization light. By transmitting the reference laser 25 MHz detuned from the transmission peak of the second UNF, the dc amplitude on the same photodiode serves as an error signal for active temperature stabilization of the UNF. Typical transmission profiles of the temperature-stabilized UNFs and the respective light-field frequencies

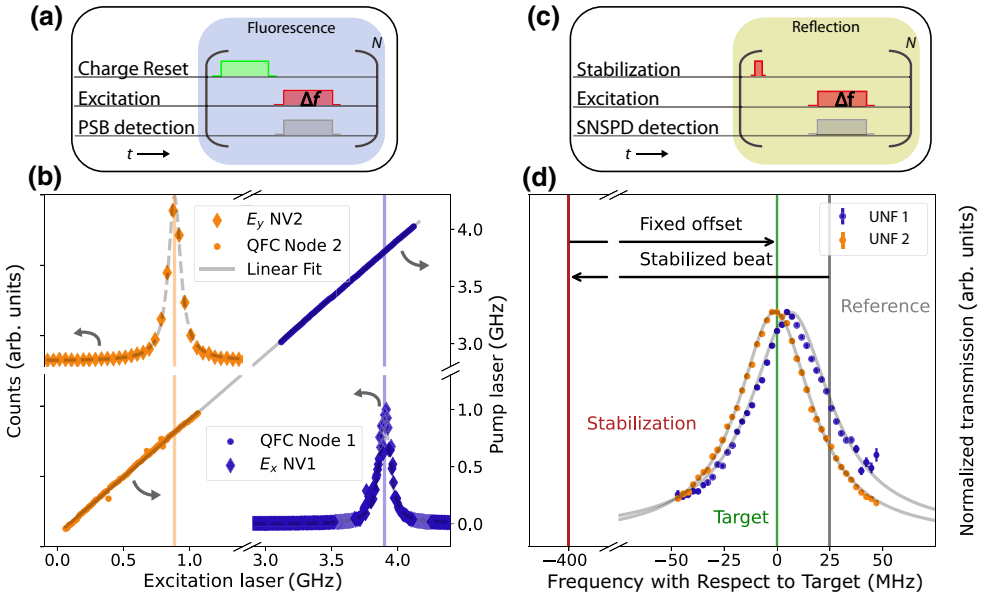

FIG. 2. The removal of spectral offset using conversion. (a) The fluorescence measurement sequence used in (b). A charge-reset pulse is followed by repeated resonant excitation, during which fluorescence in the PSB is monitored. (b) Resonant excitation spectra at node 1 (node 2) shown in blue (orange) diamonds, revealing the frequencies of the optical transitions (vertical lines) used for photon generation. The horizontal axis shows the optical excitation frequency with respect to a 470.477-THz offset. The gray dotted lines are Lorentzian fits. The right vertical axis shows the frequency of the QFC pump with respect to a 281.635-THz offset. The blue and orange dots show the QFC pump-laser frequency when the stabilization is active. The solid gray line is a linear fit. (c) A pulse schematic for measuring the transmission through the ultranarrow filter (UNF) shown in (d). Reflections from the excitation light off the sample surface, which follow the same path as the resonant NV emission, are converted to the target telecom frequency and measured on the SNSPDs. The excitation frequency is swept by modulating the AOM frequency [see Fig. 1(c)]. The transmission data are corrected for the frequency dependence of the losses in the AOMs. (d) The layout of relevant laser frequencies and the transmission data of the UNFs. The UNF transmissions (blue and orange dots) are actively stabilized via their temperature to half the transmission of the reference laser (gray vertical line). The stabilization light (red vertical line) is detuned from the target (green vertical line) and therefore reflected off the UNF (see main text).

are shown in Fig. 2(d). The small deviation from ideal peak transmission at the target frequency is due to unaccounted background voltage of the photodiode and the slight difference in the full width at half maximum (FWHM) of the two UNFs. The remaining thermal drifts of about 1 MHz have only a minor (approximately 1%) effect on the transmission (see the Supplemental Material [25]). Note that the part of the reference light that is reflected off the UNF exits the circulator toward the SNSPDs and thus needs to be taken into account when designing the experimental sequence (see Sec. IV).

We verify our frequency locking by sweeping the excitation laser and monitoring the resulting pump-laser frequency in Fig. 2(b). We observe the expected linear relationship: a change in excitation laser frequency is precisely compensated by the pump-laser frequency to always yield the same target frequency across the full tuning range. A linear fit yields the target frequency of 1587.5298 ± 0.0001 nm. This data demonstrates the ability of our frequency-locked down-conversion system to robustly compensate for a wide range of detunings.

IV. PHOTON GENERATION AT THE TARGET TELECOM WAVELENGTH

We now turn to the generation of single telecom photons by the nodes as used for the measurement of two-photon quantum interference at the midpoint. The measurement sequence involves four stages (see Fig. 3), which are synchronized across the nodes by a fixed electronic "heartbeat" every 200 μs. This heartbeat is derived from a Global-Positioning-System- (GPS) disciplined atomic clock positioned at the midpoint, which is distributed over telecom fibers via the White Rabbit precision time protocol [38]. The first 2.5 μs following each heartbeat are used for the error-signal generation for the frequency lock. This scheme allows the frequency lock to operate without knowledge of the state of the nodes, which reduces the complexity and the rounds of communication needed. Moreover, it enables the autonomous operation of each of the nodes, using their own independent hardware to control the NV center and generate single photons.

In the first stage of the measurement sequence, a charge-resonance (CR) check is performed at each node to ensure

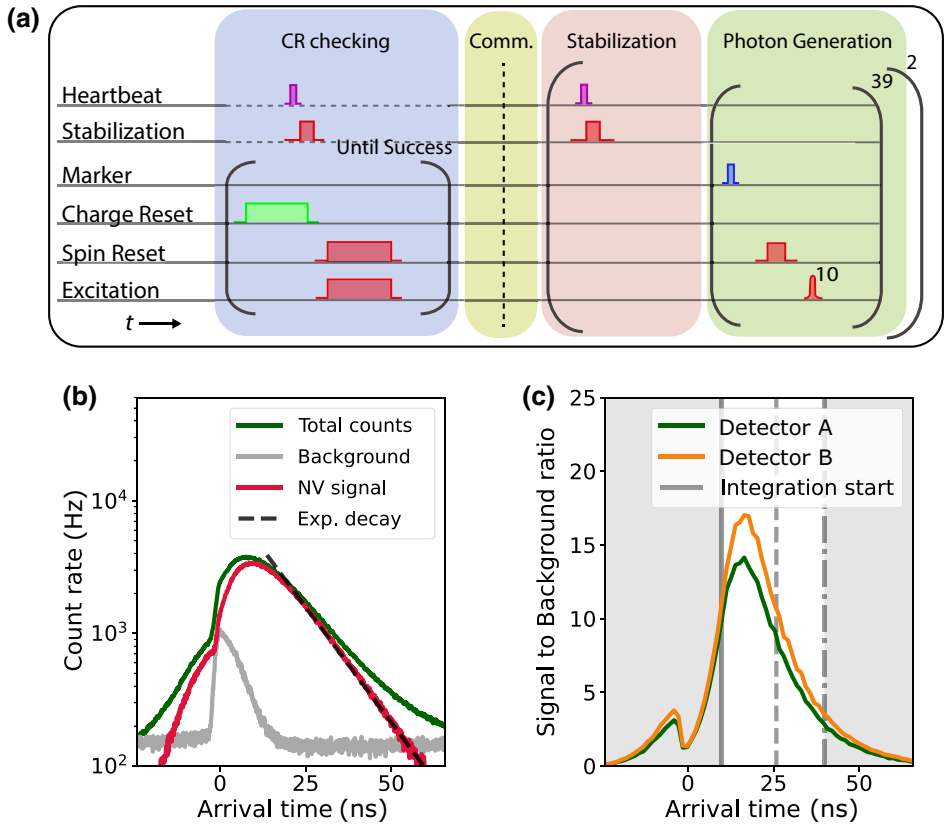

FIG. 3. The generation of single photons using a fixed heartbeat. (a) The measurement sequence for synchronized generation of single photons using a distributed heartbeat. For detailed timing, see the Supplemental Material [25]. (b) A histogram of the SNSPD counts in a single excitation round, averaged over approximately 2.8×10^{11} repetitions and analyzed in 80-ps bins. The measured count rate (green) is a combination of background (gray) and NV fluorescence (red), which is calculated by subtracting the background from the total counts. The dotted line depicts exponential decay with a 12.5-ns lifetime and serves as a guide to the eye. The NV signal before time 0, the peak of the excitation pulse, is due to the nonperfect extinction ratio of the devices generating the optical excitation pulse. The background data are taken continuously over 24 h to include any drifts that occur over the same time scale as the signal data. (c) The signal-to-background ratio (SBR) for both detectors as calculated from data in (b) (solid lines). The solid vertical gray line shows the start of our chosen detection window, whereas the dashed (dash-dotted) line shows the end for the data shown in Fig. 4(a) [Fig. 4(b)]. The difference between the two curves is due to nonequal detector performance.

that the NV centers are in the correct charge state and their transitions are on resonance with their respective spin-reset and excitation lasers [10,39]. In the event that a CR check fails, a charge-reset laser pulse is applied and a new CR check is started; this protocol is repeated until success. Importantly, the CR check can be run in parallel with the frequency locking, as the stabilization light for the lock does not reach the NV center or the local PSB detectors; hence the CR checks can run independently of the heartbeat. The second phase starts once the CR check is passed on a node, where a digital trigger from the microcontroller signals the readiness to the other node. After the readiness of both nodes has been communicated, the heartbeat at which they move to the third stage is agreed upon [Fig. 3(a)] and the Supplemental Material [25] for timings and more information.

The third stage of the measurement sequence is used for the time-multiplexed frequency stabilization, as described above. In the fourth stage, we repeatedly apply a block consisting of a spin-reset pulse (1.5 μs) followed by ten optical π pulses, ideally generating a train of ten NV photons. A time-tagged digital signal marks the times at which the photon generation takes place. This block is repeated 39 times per heartbeat period. After two heartbeat periods, the system returns to the first stage (CR checks). Note that during the third and fourth stages, time multiplexing the operations on the NV center and the error-signal generation for the frequency lock is critical, as the stabilization light and the reference light both leak into the single-photon detection path.

We analyze the resulting telecom-photon detection rate in Fig. 3(b) (green line). We show the events observed in a single detector, aggregated over all single excitation rounds and both nodes. We denote $t = 0$ as the relative time of excitation. A sharp increase in the count rate is observed when the approximately 2-ns-wide optical π

pulse starts, followed by a slower decay dominated by spontaneous emission of the NV centers.

A data set displaying only the noise counts and the counts due to leakage of the excitation π pulse (gray line) is independently generated by detuning the excitation laser by 1 GHz. The observed uniform background consists of intrinsic detector dark counts (5 Hz per detector), counts induced by detector blinding from leaked reference and stabilization light (35 Hz per detector), and SPDC photons from the QFCs (approximately 150 Hz per detector). The leakage of the excitation π pulse reflected off the sample is clearly visible. By subtracting this background from the data, we isolate the frequency-converted NV signal (red) displaying the characteristic exponential decay.

In remote-entanglement experiments, the effect of noise counts can be mitigated by defining a heralding detection-time window: only photon counts in this window are taken as valid entanglement-heralding events [10]. In general, setting the heralding window involves a trade-off between high signal to background and thus high fidelity (favoring shorter windows) and success rate (favoring longer windows). In Fig. 3(c), we plot the signal-to-background ratio (SBR) for the two detectors as a function of the photon detection time. The SBR is bounded on one side by the leaked excitation pulse and on the other side by the NV signal approaching the uniform background. For the analysis of the two-photon interference visibility [Fig. 4(a)], we apply a detection window in which the average SBR exceeds 10 (Fig. 3(c), up to dashed line). For a more detailed comparison of our model to the data [Fig. 4(b)], we use an extended window (up to the dashed-dotted line). In order to maintain the same SBR throughout the experiment, we employ a system of automatic optimization based on the live monitoring and processing of the single-photon detection events (see the Supplemental Material [25]).

V. TWO-PHOTON QUANTUM INTERFERENCE

Next, we investigate the distinguishability of the photons emitted by the two nodes by analyzing their quantum interference. For two fully indistinguishable photons impinging on the input ports of a balanced beam splitter, quantum interference leads to a vanishing probability of detecting one photon in each output port [26], while for fully distinguishable photons this probability is 0.5 [40,41]. From the (properly normalized) coincidence counts in the two detectors, we can thus extract the distinguishability of the photons.

Figure 4(a) shows the measured coincident detections between the two output arms without any background subtraction. Each excitation round is treated as a "detection bin" in which a photon can arrive. We analyze the coincidences per block of ten excitation pulses, defined as a click in both detectors in the same or two different detection bins. This leads to a maximum-detection absolute bin difference of 9 and a coincidence probability increasing linearly toward 0 bin difference. We overlay the data with a model based on independently determined parameters, treating the photons as completely distinguishable (see the Supplemental Material [25]). For the nonzero bin differences, in which the NV photons are fully distinguishable by their arrival time difference of at least 10 times the lifetime, the model shows excellent agreement with the measured coincidences. In stark contrast, we observe a strong reduction in measured coincidences compared to the model for the zero bin difference. This drop in coincidences when the photons arrive in the same bin is the hallmark of two-photon quantum interference and forms the main result of this work.

The observed visibility is defined as $V = 1 - (C_M/C_{\mathrm{dist}})$, where C_M is the measured number of coincidences and the C_{dist} are the coincidences we would have measured at zero bin difference in the event that the photons were completely distinguishable. In the inset of Fig. 4(a), we show the method of extracting the visibility. First, we use a linear fit to the total distinguishable coincidences per detection-bin difference to obtain C_E, the extrapolated coincidences for 0 bin difference. From this value we extract C_{dist}, by correcting for the imbalanced emission rates (see the Supplemental Material [25]). The resulting visibility is $V = 0.79 \pm 0.03$, which is well above the classical bound of 0.5 [40,41], proving the successful demonstration of quantum interference of single photons in the telecom L band.

A more detailed picture of the temporal shape of the coincidences allows us to test our model with more precision [Fig. 4(b)]. The accumulated coincidences for nonzero bin difference (top panel) show a characteristic shape dominated by the exponential decay of the NV emission. The data are described well by our model, which takes into account the temporal shape of the NV-NV, background-NV, and background-background coincidence contributions (derivation in the Supplemental Material [25]). The temporal histogram of coincidences within the same bin (bottom panel) shows a good match with the temporal shape predicted by our model. In particular, we observe no reduction of coincidences at 0 time delay, consistent with the visibility being limited by background counts rather than frequency differences between emitted photons [42,43].

With our knowledge of the background and signal rates, we can extract the degree of indistinguishability of the emission coming from our NV centers. We perform a Monte Carlo simulation of our data set using the independently determined parameters and apply Bayesian inference to find the most likely value of the indistinguishability, given our measured result (see the Supplemental Material [25]).

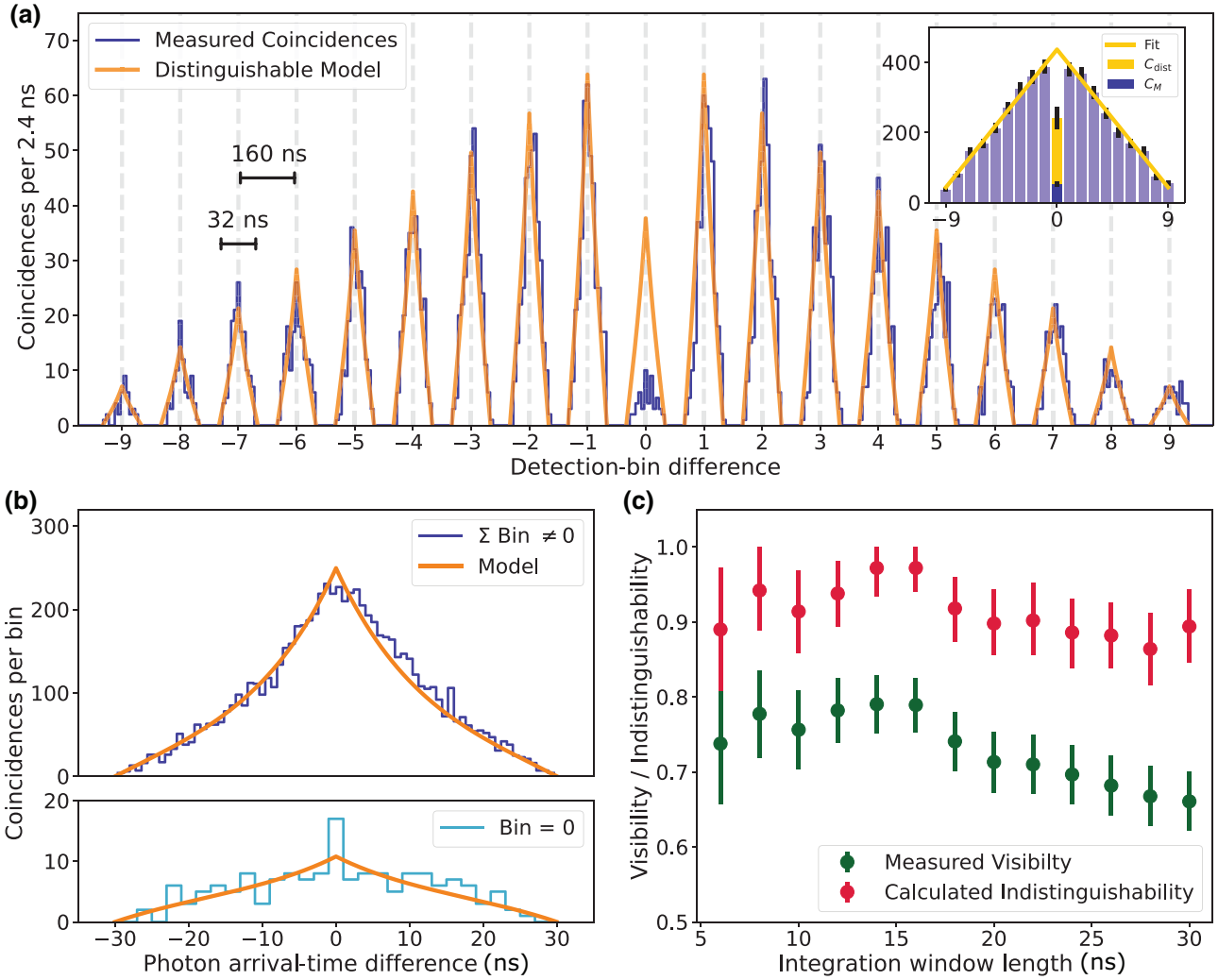

FIG. 4. Two-photon quantum interference at telecom wavelength. (a) The histogram of the measured coincidences (blue) for the analyzed time bins, overlaid with a model assuming distinguishable photons (orange), based on independently determined parameters. The histogram bin size is 2.4 ns. The vertical lines depict the time origin of each detection-bin difference. The horizontal scale bars show the relevant time scales in and between the detection-bin difference. The inset shows the extraction of the interference visibility, corrected for the imbalance of measured photons per excitation of the two nodes, using a linear fit to the total counts per bin difference (see text). (b) A histogram showing the temporal shape of the nonzero (zero) bin-difference coincidences shown in the top (bottom) panel. We overlay the data with the same model (see the Supplemental Material [25]), taking into account brightness and background rates and the indistinguishability of converted NV photons of 0.9 [see (c)]. The bin size for the top (bottom) panel is 0.8 ns (2 ns). (c) The measured visibility and extracted indistinguishability of converted NV photons for varying window length. The error bars for visibility and indistinguishability are 1σ and a 68% confidence interval, respectively. The green (blue) circled points indicate data corresponding to the window length shown in Fig. 4(a) [Fig. 4(b)].

In Fig. 4(c), we plot the visibility and the extracted photon indistinguishability for increasing detection-time-window lengths. While the visibility drops for longer windows consistent with the decreasing SBR, the indistinguishability of the NV photons remains high, at around 0.9. We note that this latter value is similar to values found for NV-NV two-photon quantum interference without frequency conversion [11], confirming that our conversion scheme, including the frequency stabilization to a single target wavelength, preserves the original photon indistinguishability and enables solid-state entanglement generation via entanglement swapping.

VI. CONCLUSION AND OUTLOOK

We show quantum interference of single photons emitted by spectrally distinct NV centers, by converting them to the same telecom wavelength. We demonstrate an actively stabilized QFC scheme using DFG on fully independent nodes. The design and implementation allow for

the scheme to be used at large distances. Furthermore, the techniques can be readily transferred to other quantum emitters in the visible regime with minimal adaptations to the conversion optics and control schemes used.

Future improvements to our system can increase the performance in multiple ways. First, adapting our optical design to prevent detector blinding by the stabilization light can lower the detector contribution to the background counts to the design level of 5 Hz. Second, a different approach [44] to the QFC technique based on a bulk crystal may remove the (currently dominant) SPDC background noise due to poling irregularities. Third, the signal level of collected coherent photons from the NV centers could be improved significantly by the use of an open microcavity [45,46]. In particular, achieving a fraction of coherent emission of 46% as reported in Ref. [45] would raise the SBR to above 200. Finally, by extending the hardware, we can stabilize the optical phase of the single photons emitted by the NV centers, enabling entanglement generation upon heralding of a single photon [23].

By combining the protocols demonstrated here with established spin-photon entangling operations and photon heralding at the midpoint [10,11], remote NV centers can be projected in an entangled state via telecom photons. Owing to the low propagation loss of these photons and the extendable control scheme, our results pave the way for entanglement between solid-state qubits over deployed fiber at metropolitan scale.

The data sets that support this paper and the software to analyze them are available at 4TU.ResearchData [47].

ACKNOWLEDGMENTS

We would like to acknowledge Matthew Weaver and Matteo Pompili for fruitful discussions during the model development and data analysis and Ludo Visser and Pieter Botma for software support during the measurements. We thank Martin Eschen and Boudewijn van den Bosch for their contributions to building and maintaining parts of the setup and Wouter Koek for simulations aiding the design. We thank Klaas Jan de Kraker, Sander Kossen, and Emanuele Uccelli for managing many tasks in the project and sample production. We thank Ruud Schmits and Jacob Dalle for their contributions to the sample production-process development. We acknowledge funding from the Dutch Research Council (NWO) through the project "QuTech Part II Applied-oriented research" (Project No. 601.QT.001), a Vici grant (Project No. 680-47-624), and the Zwaartekracht program Quantum Software Consortium (Project No. 024.003.037/3368). We further acknowledge funds from the Dutch Ministry of Economic Affairs and Climate Policy (EZK), as part of the Quantum Delta NL program, and Holland High Tech through the TKI HTSM (20.0052 PPS) funds.

A.S., K.L.vd.E., E.v.Z., and R.H. devised the experiment. J.M., A.V., R.A.J. H, A.K., and B.B. designed and built the experimental hardware and the frequency-conversion modules. S.C., J.v.R., and I.t.R. developed the measurement, timing, and control software framework. M.M. and A.M.E. grew and prepared the diamond-device substrates. R.V., A.S., and J.M. characterized and fabricated the diamond devices. A.S., K.L.vd.E., M.C.R., and S.O.F. carried out the experiments and collected the data. A.T., A.S., and M.C.R. developed supporting simulations. A.S., K.L.vd.E., and M.C.R. analyzed the data. A.S. and R.H. wrote the main manuscript with input from K.L.vd.E, and M.C.R. A.S., K.L.vd.E., and M.C.R. wrote the Supplemental Material. All authors commented on the manuscript. J.M. and E.v.Z. coordinated the experimental work. R.H. supervised the quantum experiments.

[1] H. J. Kimble, The quantum Internet, Nature **453**, 1023 (2008).

[2] S. Wehner, D. Elkouss, and R. Hanson, Quantum Internet: A vision for the road ahead, Science **362**, eaam9288 (2018).

[3] A. Ekert and R. Renner, The ultimate physical limits of privacy, Nature **507**, 443 (2014).

[4] L. Jiang, J. M. Taylor, A. S. Sørensen, and M. D. Lukin, Distributed quantum computation based on small quantum registers, Phys. Rev. A, **76**, 062323 (2007).

[5] D. Gottesman, T. Jennewein, and S. Croke, Longer-Baseline Telescopes Using Quantum Repeaters, Phys. Rev. Lett. **109**, 070503 (2012).

[6] D. L. Moehring, P. Maunz, S. Olmschenk, K. C. Younge, D. N. Matsukevich, L.-M. Duan, and C. Monroe, Entanglement of single-atom quantum bits at a distance, Nature **449**, 68 (2007).

[7] S. Ritter, C. Nölleke, C. Hahn, A. Reiserer, A. Neuzner, M. Uphoff, M. Mücke, E. Figueroa, J. Bochmann, and G. Rempe, An elementary quantum network of single atoms in optical cavities, Nature **484**, 195 (2012).

[8] J. Hofmann, M. Krug, N. Ortegel, L. Gérard, M. Weber, W. Rosenfeld, and H. Weinfurter, Heralded entanglement between widely separated atoms, Science **337**, 72 (2012).

[9] L. Stephenson, D. Nadlinger, B. Nichol, S. An, P. Drmota, T. Ballance, K. Thirumalai, J. Goodwin, D. Lucas, and C. Ballance, High-Rate, High-Fidelity Entanglement of Qubits Across an Elementary Quantum Network, Phys. Rev. Lett. **124**, 110501 (2020).

[10] H. Bernien, B. Hensen, W. Pfaff, G. Koolstra, M. S. Blok, L. Robledo, T. H. Taminiau, M. Markham, D. J. Twitchen, L. Childress, and R. Hanson, Heralded entanglement between solid-state qubits separated by three metres, Nature **497**, 86 (2013).

[11] P. C. Humphreys, N. Kalb, J. P. J. Morits, R. N. Schouten, R. F. L. Vermeulen, D. J. Twitchen, M. Markham, and R. Hanson, Deterministic delivery of remote entanglement on a quantum network, Nature **558**, 268 (2018).

[12] A. Delteil, Z. Sun, W.-b. Gao, E. Togan, S. Faelt, and A. Imamoğlu, Generation of heralded entanglement between distant hole spins, Nat. Phys. **12**, 218 (2016).
[13] R. Stockill, M. Stanley, L. Huthmacher, E. Clarke, M. Hugues, A. Miller, C. Matthiesen, C. Le Gall, and M. Atatüre, Phase-Tuned Entangled State Generation between Distant Spin Qubits, Phys. Rev. Lett. **119**, 010503 (2017).
[14] I. Usmani, C. Clausen, F. Bussières, N. Sangouard, M. Afzelius, and N. Gisin, Heralded quantum entanglement between two crystals, Nat. Photonics **6**, 234 (2012).
[15] M. l. G. Puigibert, M. F. Askarani, J. H. Davidson, V. B. Verma, M. D. Shaw, S. W. Nam, T. Lutz, G. C. Amaral, D. Oblak, and W. Tittel, Entanglement and nonlocality between disparate solid-state quantum memories mediated by photons, Phys. Rev. Res. **2**, 013039 (2020).
[16] D. Lago-Rivera, S. Grandi, J. V. Rakonjac, A. Seri, and H. de Riedmatten, Telecom-heralded entanglement between multimode solid-state quantum memories, Nature **594**, 37 (2021).
[17] C. W. Chou, H. de Riedmatten, D. Felinto, S. V. Polyakov, S. J. van Enk, and H. J. Kimble, Measurement-induced entanglement for excitation stored in remote atomic ensembles, Nature **438**, 828 (2005).
[18] Y. Yu, F. Ma, X.-Y. Luo, B. Jing, P.-F. Sun, R.-Z. Fang, C.-W. Yang, H. Liu, M.-Y. Zheng, X.-P. Xie, W.-J. Zhang, L.-X. You, Z. Wang, T.-Y. Chen, Q. Zhang, X.-H. Bao, and J.-W. Pan, Entanglement of two quantum memories via fibres over dozens of kilometres, Nature **578**, 240 (2020).
[19] R. Riedinger, S. Hong, R. A. Norte, J. A. Slater, J. Shang, A. G. Krause, V. Anant, M. Aspelmeyer, and S. Gröblacher, Non-classical correlations between single photons and phonons from a mechanical oscillator, Nature **530**, 313 (2016).
[20] D. Hucul, I. V. Inlek, G. Vittorini, C. Crocker, S. Debnath, S. M. Clark, and C. Monroe, Modular entanglement of atomic qubits using photons and phonons, Nat. Phys. **11**, 37 (2015).
[21] V. Krutyanskiy, M. Meraner, J. Schupp, V. Krcmarsky, H. Hainzer, and B. P. Lanyon, Light-matter entanglement over 50 km of optical fibre, NPJ Quantum Inf. **5**, 72 (2019).
[22] S. Daiss, S. Langenfeld, S. Welte, E. Distante, P. Thomas, L. Hartung, O. Morin, and G. Rempe, A quantum-logic gate between distant quantum-network modules, Science **371**, 614 (2021).
[23] M. Pompili, S. L. N. Hermans, S. Baier, H. K. C. Beukers, P. C. Humphreys, R. N. Schouten, R. F. L. Vermeulen, M. J. Tiggelman, L. dos Santos Martins, B. Dirkse, S. Wehner, and R. Hanson, Realization of a multinode quantum network of remote solid-state qubits, Science **372**, 259 (2021).
[24] T. van Leent, M. Bock, F. Fertig, R. Garthoff, S. Eppelt, Y. Zhou, P. Malik, M. Seubert, T. Bauer, W. Rosenfeld, W. Zhang, C. Becher, and H. Weinfurter, Entangling single atoms over 33 km telecom fibre, 2021.
[25] See the Supplemental Material at http://link.aps.org/supplemental/10.1103/PRXQuantum.3.020359 for a detailed overview of the experimental setup, modeling of the expected visibilities, detailed information on the data processing, and more details on the performance of the single-photon filtering and detection.
[26] C. K. Hong, Z. Y. Ou, and L. Mandel, Measurement of Subpicosecond Time Intervals between Two Photons by Interference, Phys. Rev. Lett. **59**, 2044 (1987).
[27] M. L. Goldman, M. W. Doherty, A. Sipahigil, N. Y. Yao, S. D. Bennett, N. B. Manson, A. Kubanek, and M. D. Lukin, State-selective intersystem crossing in nitrogen-vacancy centers, Phys. Rev. B **91**, 165201 (2015).
[28] N. Kalb, P. C. Humphreys, J. J. Slim, and R. Hanson, Dephasing mechanisms of diamond-based nuclear-spin memories for quantum networks, Phys. Rev. A **97**, 062330 (2018).
[29] A. Tchebotareva, S. L. N. Hermans, P. C. Humphreys, D. Voigt, P. J. Harmsma, L. K. Cheng, A. L. Verlaan, N. Dijkhuizen, W. de Jong, A. Dréau, and R. Hanson, Entanglement between a Diamond Spin Qubit and a Photonic Time-Bin Qubit at Telecom Wavelength, Phys. Rev. Lett. **123**, 063601 (2019).
[30] J. Pelc, C. Langrock, Q. Zhang, and M. Fejer, Influence of domain disorder on parametric noise in quasi-phase-matched quantum frequency converters, Opt. Lett. **35**, 2804 (2010).
[31] M. Ruf, M. IJspeert, S. van Dam, N. de Jong, H. van den Berg, G. Evers, and R. Hanson, Optically coherent nitrogen-vacancy centers in micrometer-thin etched diamond membranes, Nano Lett. **19**, 3987 (2019).
[32] S. Meesala, Y.-I. Sohn, B. Pingault, L. Shao, H. A. Atikian, J. Holzgrafe, M. Gündoğan, C. Stavrakas, A. Sipahigil, C. Chia, R. Evans, M. J. Burek, M. Zhang, L. Wu, J. L. Pacheco, J. Abraham, E. Bielejec, M. D. Lukin, M. Atatüre, and M. Lončar, Strain engineering of the silicon-vacancy center in diamond, Phys. Rev. B **97**, 205444 (2018).
[33] A. Sipahigil, R. E. Evans, D. D. Sukachev, M. J. Burek, J. Borregaard, M. K. Bhaskar, C. T. Nguyen, J. L. Pacheco, H. A. Atikian, C. Meuwly, R. M. Camacho, F. Jelezko, E. Bielejec, H. Park, M. Lončar, and M. D. Lukin, An integrated diamond nanophotonics platform for quantum-optical networks, Science **354**, 847 (2016).
[34] S. Sun, J. L. Zhang, K. A. Fischer, M. J. Burek, C. Dory, K. G. Lagoudakis, Y.-K. Tzeng, M. Radulaski, Y. Kelaita, A. Safavi-Naeini, Z.-X. Shen, N. A. Melosh, S. Chu, M. Lončar, and J. Vučković, Cavity-Enhanced Raman Emission from a Single Color Center in a Solid, Phys. Rev. Lett. **121**, 083601 (2018).
[35] J. H. Weber, B. Kambs, J. Kettler, S. Kern, J. Maisch, H. Vural, M. Jetter, S. L. Portalupi, C. Becher, and P. Michler, Two-photon interference in the telecom C-band after frequency conversion of photons from remote quantum emitters, Nat. Nanotechnol. **14**, 23 (2019).
[36] X. You *et al.*, Quantum interference between independent solid-state single-photon sources separated by 300 km fiber. arXiv:2106.15545 [quant-ph], (2021).
[37] C. E. Bradley, J. Randall, M. H. Abobeih, R. C. Berrevoets, M. J. Degen, M. A. Bakker, M. Markham, D. J. Twitchen, and T. H. Taminiau, A Ten-Qubit Solid-State Spin Register with Quantum Memory up to One Minute, Phys. Rev. X **9**, 031045 (2019).
[38] E. F. Dierikx, A. E. Wallin, T. Fordell, J. Myyry, P. Koponen, M. Merimaa, T. J. Pinkert, J. C. J. Koelemeij,

H. Z. Peek, and R. Smets, White Rabbit precision time protocol on long-distance fiber links, IEEE Trans. Ultrason. Ferroelectr. Freq. Control **63**, 945 (2016).

[39] L. Robledo, L. Childress, H. Bernien, B. Hensen, P. F. A. Alkemade, and R. Hanson, High-fidelity projective read-out of a solid-state spin quantum register, Nature **477**, 574 (2011).

[40] H. Paul, Interference between independent photons, Rev. Mod. Phys. **58**, 209 (1986).

[41] F. Bouchard, A. Sit, Y. Zhang, R. Fickler, F. M. Miatto, Y. Yao, F. Sciarrino, and E. Karimi, Two-photon interference: The Hong-Ou-Mandel effect, Rep. Prog. Phys. **84**, 012402 (2021).

[42] T. Legero, T. Wilk, A. Kuhn, and G. Rempe, Time-resolved two-photon quantum interference, Appl. Phys. B **77**, 797 (2003).

[43] B. Kambs and C. Becher, Limitations on the indistinguishability of photons from remote solid state sources, New J. Phys. **20**, 115003 (2018).

[44] J. F. Geus, F. Elsen, S. Nyga, B. Jungbluth, H.-D. Hoffmann, and C. Haefner, in *Quantum Computing, Communication, and Simulation II* (P. R. Hemmer and A. L. Migdall, eds.), International Society for Optics and Photonics, (SPIE, 2022), vol. 12015, p. 24.

[45] D. Riedel, I. Söllner, B. J. Shields, S. Starosielec, P. Appel, E. Neu, P. Maletinsky, and R. J. Warburton, Deterministic Enhancement of Coherent Photon Generation from a Nitrogen-Vacancy Center in Ultrapure Diamond, Phys. Rev. X **7**, 031040 (2017).

[46] M. Ruf, M. Weaver, S. van Dam, and R. Hanson, Resonant Excitation and Purcell Enhancement of Coherent Nitrogen-Vacancy Centers Coupled to a Fabry-Perot Microcavity, Phys. Rev. Appl. **15**, 024049 (2021).

[47] A. Stolk, K. L. Van der Enden, M.-C. Roehsner, A. Teepe, C. Bradley, S. Cadot, R. Hagen, A. Khorev, R. Vollmer, and A. Edmonds *et al.*, Data for: "Telecom-band quantum interference of frequency-converted photons from remote detuned NV centers" 4TU.ResearchData, https://doi.org/10.1103/PRXQuantum.3.020359 (2022).